



# CHORUS

This is the accepted manuscript made available via CHORUS. The article has been published as:

## Atomistic fracture energy partitioning at a metal-ceramic interface using a nanomolecular monolayer

Ashutosh Jain, Binay Singh, Saurabh Garg, N. Ravishankar, Michael Lane, and Ganpati Ramanath

Phys. Rev. B **83**, 035412 — Published 20 January 2011

DOI: [10.1103/PhysRevB.83.035412](https://doi.org/10.1103/PhysRevB.83.035412)

# Atomistic fracture energy partitioning at a metal-ceramic interface using a nanomolecular monolayer

Ashutosh Jain<sup>1</sup>, Binay Singh<sup>1</sup>, Saurabh Garg<sup>1</sup>, N. Ravishankar<sup>1</sup>, Michael Lane<sup>2</sup>, Ganpati Ramanath<sup>1\*</sup>

<sup>1</sup>*Rensselaer Polytechnic Institute, Materials Science & Engineering Dept., Troy, NY, 12180, USA*

<sup>2</sup>*Emory and Henry College, Chemistry Department, Emory, VA 24327, USA.*

## ABSTRACT

We report an experimental approach to partition the fracture energy of a metal-ceramic interface into work of adhesion and plasticity, unveiling the nanomechanics of interfacial deformation and fracture. We obviate crack path uncertainties by constraining fracture to occur in an interfacial nanomolecular layer through fissure of a single bond type whose strength is varied by adjusting the chemical environment. This approach is adaptable for studying interfacial fracture and related phenomena in diverse materials systems in different thermochemical environments.

---

\*Corresponding author: [ramanath@rpi.edu](mailto:ramanath@rpi.edu)

## I. INTRODUCTION

The partitioning of interface fracture energy into bond breaking energy and plastic energy in ductile layer(s) constituting the interface is a central problem in fracture mechanics. Fracture energy (or toughness)  $\Gamma_{FT}$  is typically comprised of multiple processes such as bond-breaking<sup>1</sup>, corrosion<sup>2</sup>, and crack-tip plastic flow and repair<sup>3,4</sup>. The Griffith and Irwin model<sup>1,3</sup> partitions  $\Gamma_{FT}$  into two terms  $\gamma_a$  and  $\gamma_p$ :  $\Gamma_{FT} = \gamma_a + \gamma_p$ , where  $\gamma_a$  is the work of adhesion, and  $\gamma_p$  is the plastic energy which is a function of  $\gamma_a$ . Cohesive fracture in homogenous bulk materials has been studied for many decades and empirical descriptions of fracture have been developed by approximating  $\Gamma_{FT} \sim \gamma_a$  for brittle materials ( $\gamma_p \sim 0$ ), and  $\Gamma_{FT} \sim \gamma_p$  for ductile materials ( $\gamma_p \gg \gamma_a$ ). However, currently there are no models that incorporate experimentally-validated  $\gamma_a$  and  $\gamma_p$  terms to obtain realistic atomistic descriptions of fracture at interfaces comprised of both brittle and ductile materials, i.e., where  $\gamma_a$  and  $\gamma_p$  are comparable and neither term can be neglected. Characterizing interfacial fracture has remained an exacting experimental challenge due to uncertainties in crack path and types of bonds broken. Although factors such as film thickness, crack tip reaction kinetics and humidity are known to influence fracture energy<sup>5,6</sup>, quantitative partitioning of  $\Gamma_{FT}$  in terms of specific atomistic processes has been elusive. As a result, current atomistic descriptions of interfacial fracture energetics are primarily based on theoretical models and computer simulations<sup>7,8</sup>.

Here, we demonstrate an experimental approach to partition  $\Gamma_{FT}$  of a metal-ceramic interface by using a nanomolecular monolayer (NML) at the interface. Crack path uncertainties are obviated by constraining fracture to occur through the fissure of only one bond type in the NML at the interface. Additionally, we vary the interfacial bond strength, and hence  $\gamma_a$ , by controlling the chemical environment, thereby allowing  $\gamma_p$  determination by measuring  $\Gamma_{FT}$ . We illustrate this approach for a model copper-silica interface treated with an organosilane NML where bond-breaking occurs by siloxane bridge hydrolysis. This method could be adapted for studying interface fracture and related phenomena in

different thermochemical environments, e.g., stress corrosion cracking, electromigration and stress-induced voiding, in a variety of materials systems through appropriate choice of NMLs.

## II. EXPERIMENTAL DETAILS

Our test structures consisted of a copper-silica interface functionalized with a 0.7-nm-thick NML comprised of mercapto-propyl-tri-methoxy-silane (MPTMS) molecules. NMLs were formed on Si(001) wafers capped with an 85-nm-thick silica by dipping the wafers in a 5 mM MPTMS in toluene for 30 min in flowing N<sub>2</sub> as described previously<sup>9, 10</sup>. A 35-nm-thick Cu layer was deposited on the NML/SiO<sub>2</sub>/Si(001) followed by a 150-nm-thick Ta layer in a CVC DC sputter system with a 5 x 10<sup>-7</sup> Torr base pressure. The samples were annealed at 300 °C for 30 min, and the Ta/Cu/NML/SiO<sub>2</sub>/Si(001) was bonded to a dummy Si wafer with an epoxy, for four point bend tests. The Ta layer was used to offset poor Cu-epoxy adhesion. Our earlier works<sup>9, 10</sup> have shown that the NML is strongly bound to the copper overlayer via thioligation and bond-breaking occurs exclusively at the NML-silica interface through the fissure of Si-O-Si bridges formed during molecular assembly (Fig. 1a). We vary  $\gamma_a$  through moisture control by exploiting the sensitivity of siloxane bonds to hydrolysis<sup>9, 11</sup>.

We determined the fracture energy of thin film sandwiches with Cu/NML/SiO<sub>2</sub> interfaces by four-point-bend tests carried out *in situ* in environments with different water activity  $0.2 \leq a_{\text{H}_2\text{O}} \leq 0.8$  and temperature  $278 \text{ K} \leq T \leq 358 \text{ K}$  in a CSZ PZ series chamber. We note that  $a_{\text{H}_2\text{O}}$  is identical to relative humidity, and represents the water chemical potential  $\mu_{\text{H}_2\text{O}}$  when plotted on a log scale (as we have), because  $\mu_{\text{H}_2\text{O}} = NRT \log a_{\text{H}_2\text{O}}$ , where R is the gas constant and T the absolute temperature, and N the number of interfacial bonds per unit area. We strained 5 mm x 40 mm rectangular beams of Si/epoxy/Ta/Cu/NML/SiO<sub>2</sub>/Si(001) stacks at a 10 nm/s displacement until a crack emerging from a fine notch scribed on the Si substrate propagated to the weakest interface (see green line in Fig. 1b), an event indicated by the first plateau in the load-displacement curve corresponding to a critical driving energy  $\Gamma_c$ .

At the plateau, we halted the externally applied displacement to determine the minimum sub-critical energy required for crack propagation (see red line in Fig. 1b). The delamination velocity  $v$  decreases monotonically and approaches zero as the remnant driving energy  $\Gamma$  diminishes to a threshold value that corresponds to the fracture toughness  $\Gamma_{FT}$  at equilibrium of the atomistic process that drives the crack. Thus,  $\Gamma_{FT}$  is extracted from  $v$ - $\Gamma$  curves as  $v \rightarrow 0$  and  $d\Gamma/dt \rightarrow 0$  as described elsewhere<sup>12</sup>. In our tests, the phase angle was  $\sim 43^\circ$  corresponding to approximately equal parts of shear and normal loading at the interface<sup>13</sup>. Each  $\Gamma_{FT}$  value reported here is an average of at least four tests; the error bars denote one standard deviation.

Fracture surfaces were analyzed by X-ray photoelectron spectroscopy (XPS) to determine the fracture path and obtain insights into the bond-breaking mechanism. XPS measurements were carried out in a PHI 5400 instrument with a Mg K $\alpha$  beam at a 23.5 eV analyzer pass energy. Charging-induced spectral shifts were corrected by using the adventitious C 1s peak at 285 eV as an internal calibration.

### III. RESULTS AND DISCUSSION

Fracture toughness tests show that  $\Gamma_{FT}$  is a strong function of both temperature and water activity  $a_{H_2O}$  (see Figs. 2a-b). Specifically,  $\Gamma_{FT}$  decreases with increasing  $a_{H_2O}$  at constant temperature as well as with increasing temperature at constant  $a_{H_2O}$ . The latter is due to an increase in the water vapor pressure  $p_{H_2O}$  driven by an increase in saturation vapor pressure  $p_{sat}$  with temperature ( $a_{H_2O} = p_{H_2O}/p_{sat}$ )<sup>14</sup>, consistent with previous studies of Cu/TaN/SiO<sub>2</sub> interfaces<sup>5</sup>. We attribute the  $\Gamma_{FT}$  decrease with  $a_{H_2O}$  to water-induced siloxane bridge fissure at the interface similar to stress corrosion cracking in glasses<sup>15</sup> as corroborated by fracture surface spectroscopy measurements. XPS spectra from Cu fracture surfaces show the Si 2p core-level band at  $\sim 102.5$  eV characteristic of silyl alkyl moieties in the organosilane, in contrast to the silica Si 2p signature at  $\sim 103.5$  eV seen on silica fracture surfaces (see Fig. 3), confirming that delamination occurs via siloxane bond fissure at the NML-silica interface<sup>10</sup>. This delamination pathway remains

unchanged for  $0.05 \leq a_{\text{H}_2\text{O}} < 0.8$ , as seen from fracture surfaces showing essentially identical spectral features. At the highest water activity in our experiments, i.e.,  $a_{\text{H}_2\text{O}} \sim 0.8$ , Cu fracture surfaces exhibit a silica sub-band along with a prominent the silyl alkyl signature, suggesting some fracture path deviation due to bond breaking in the silica substrate.

Plotting  $\Gamma_{\text{FT}}$  as a function of  $a_{\text{H}_2\text{O}}$  for  $T = 293$  K reveals two distinct regimes separable at  $a_{\text{H}_2\text{O}} \sim 0.5$ - $0.4$  (see Fig. 4a). For  $a_{\text{H}_2\text{O}} \leq 0.4$ , Cu/NML/silica interfaces exhibit  $\Gamma_{\text{FT}}$  ranging from  $\sim 2.1$  to  $3.6$   $\text{J/m}^2$ , which are comparable or significantly higher than  $\gamma_a \sim 1.75$   $\text{J/m}^2$  reported for fused silica<sup>16</sup>, pointing to the existence of secondary energy dissipation processes such as copper plasticity. The twofold higher magnitude of  $d\Gamma_{\text{FT}}/d\log a_{\text{H}_2\text{O}}$  for  $a_{\text{H}_2\text{O}} < 0.4$ - $0.5$  than that observed at higher  $a_{\text{H}_2\text{O}}$  allows us to separate the relative extents of  $\gamma_a$  and  $\gamma_p$  at the Cu/NML/silica interface.

At high moisture contents, e.g., for  $a_{\text{H}_2\text{O}} > 0.4$ , the main energy dissipation mechanism is siloxane bond fissure via hydrolysis through the reaction  $\text{Si-O-Si} + \text{H}_2\text{O} \rightarrow 2 \text{Si-OH}$ , implying that  $\Gamma_{\text{FT}} = \gamma_a$ . The linear behavior of  $\Gamma_{\text{FT}}$  with  $\log a_{\text{H}_2\text{O}}$  is reminiscent of the linear dependence of the equilibrium free energy of this reaction on  $\log a_{\text{H}_2\text{O}}$ <sup>17</sup> that yields the interfacial Si-O-Si bond density  $N_{\text{Si-O-Si}}$ , and hence  $\gamma_a$ . Thus,  $\log a_{\text{H}_2\text{O}}$  serves as a proxy for  $\gamma_a$ . Using  $d\gamma_a/d\log a_{\text{H}_2\text{O}} = N_{\text{Si-O-Si}}RT$ , we get  $N_{\text{Si-O-Si}} = 2 \times 10^{20}$   $\text{m}^{-2}$ , which agrees well with  $N_{\text{Si-O-Si}} = 0.7 \times 10^{20}$   $\text{m}^{-2}$  obtained by fitting  $v$ - $\Gamma$  characteristics for different  $a_{\text{H}_2\text{O}}$  to a reaction rate kinetics model for water-induced fracture in orthosilicates<sup>15, 18</sup>. The fit also yields a crack propagation activation energy of  $\sim 0.3$  eV/bond reported for siloxane hydrolysis, confirming that  $\Gamma_{\text{FT}} = \gamma_a$  for  $a_{\text{H}_2\text{O}} > 0.4$ .

The abrupt increase in the slope  $d\Gamma_{\text{FT}}/d\log a_{\text{H}_2\text{O}}$  below  $a_{\text{H}_2\text{O}} \sim 0.5$ - $0.4$  reflects the onset of an additional energy dissipation mechanism, identified to be copper plasticity. We discount the possibility of deformation in the silica layer because this mechanism is operative only above  $900$   $^\circ\text{C}$ <sup>19</sup>. If copper

plasticity is responsible for the higher  $d\Gamma_{FT}/d\log a_{H_2O}$  for  $a_{H_2O} < 0.4$ , the copper film should yield at  $a_{H_2O} \sim 0.4-0.5$ . To verify this requirement, we further examined the threshold work of adhesion  $\gamma_0$  ( $= \gamma_a = \Gamma_{FT}$  at yield point) value of  $\sim 2 \text{ J/m}^2$  and estimated the yield stress  $\sigma_y$  from the strain energy per unit volume at  $a_{H_2O} \sim 0.4-0.5$ . Since the loading phase angle in our four point bend tests is  $\sim 43^\circ$ , the normal and shear mode components are roughly equal, i.e.,  $\Gamma_I \sim \Gamma_{II} \sim \frac{\gamma_0}{2} \sim 1 \text{ J/m}^2$ . This value is in good agreement with the dislocation emission energy of  $\sim 0.84 \text{ J/m}^2$  for mode I yielding according to the Rice-Thompson description<sup>20</sup>, and is consistent with the expectation that  $\Gamma_I$  is the main contributor to interfacial bond cleavage and plasticity whilst  $\Gamma_{II}$  accounts for frictional effects. The yield stress  $\sigma_y$  calculated from  $\Gamma_I \sim \frac{\gamma_0}{2}$  for different copper thicknesses by assuming copper stiffness  $E=130 \text{ GPa}$ <sup>21</sup> are within  $\sim 15-30\%$  of  $\sigma_y$  obtained from nanoindentation measurements (see Fig. 4b), confirming that  $d\Gamma_{FT}/d\log a_{H_2O}$  increase for  $a_{H_2O} < 0.4$  is due to copper plastic deformation. Moreover, the observed linear increase in  $\Gamma_{FT}$  with  $\log a_{H_2O}$  for  $a_{H_2O} < 0.4$  (Fig. 4a) is consistent with increased plastic deformation because the plastic zone size  $R_0$  is expected to scale linearly with  $\gamma_a$  (and hence  $\log a_{H_2O}$ ) as<sup>22</sup>  $R_0 = \frac{E\gamma_a}{3\pi(1-\nu^2)\sigma_y^2}$  for constant  $\sigma_y$ , where  $\nu$  is the Poisson's ratio. Finally, our observation of  $\Gamma_{FT}$  increase with Cu film thickness (see Fig. 5c) for a fixed  $a_{H_2O}$  in the region  $a_{H_2O} < 0.4$  regime also confirms copper plasticity because lower  $\sigma_y$  and larger plastic zones in thicker films are expected to abet plastic deformation<sup>21,23</sup>.

The above discussion indicates that measuring  $\Gamma_{FT}$  as a function of  $\log a_{H_2O}$  (or  $\mu_{H_2O}$ ) could be an attractive alternative way of determining thin film yield stress. The  $\sigma_y$  values extracted from  $\Gamma_{FT}$ - $\log a_{H_2O}$  characteristics are similar to, but consistently lower than, that from nanoindentation (Fig. 4b), and higher than that predicted by molecular dynamics simulations<sup>24</sup> of nanograined bulk copper as well as extrapolations of nanoindentation results from thicker films<sup>25</sup>. These results suggests that obtaining  $\sigma_y$  by

our method mitigates the so-called substrate effect invoked to explain high  $\sigma_y$  obtained from nanoindentation of sub-200-nm-thick films.

For  $a_{\text{H}_2\text{O}} < \sim 0.4$ , fracture toughness  $\Gamma_{\text{FT}}$  includes non-negligible contributions from both  $\gamma_a$  and  $\gamma_p$ . We can calculate  $\gamma_p$  by calculating the difference between the measured toughness  $\Gamma_{\text{FT}}$  and the  $\gamma_a$  obtained by extrapolating the  $\gamma_a$  vs.  $\log a_{\text{H}_2\text{O}}$  linear fit for high  $a_{\text{H}_2\text{O}}$  to the  $a_{\text{H}_2\text{O}} < 0.4$  regime. This extrapolation is justified because  $\gamma_a$  is sensitive only to  $a_{\text{H}_2\text{O}}$ , as described earlier. Thus, we can plot  $\gamma_p$  as a function of  $\gamma_a$  (see Fig. 5a) by the equation  $\gamma_p = \tau(\gamma_a - \gamma_0)$ , where  $\gamma_0 = \gamma_a$  at yield point. For  $\gamma_a < \gamma_0$ , the plastic energy  $\gamma_p = \tau = 0$ , and for  $\gamma_a > \gamma_0$ ,  $\gamma_p$  increases linearly with  $\gamma_a$  with  $\tau \sim 1.2$ . Therefore, besides separating the contributions of the work of adhesion and plasticity, our results reveal the quantitative dependence of  $\gamma_p$  on  $\gamma_a$ . While a multiplicative effect has been postulated<sup>26</sup>, and analytical models predict  $0.2 < \tau < 8$  for hetero-interfaces<sup>21</sup>, our experimental results here provide a new means for directly determining  $\tau$ . Earlier experimental works<sup>27-30</sup> based on a dislocation model and measurement of Cu films with different thicknesses have also related  $\gamma_p$  and  $\gamma_a$ . But, our approach obviates complications of yield stress variations in films of different thicknesses and offers versatility for studying the effects of environmental degradation, segregation, and molecular functionalization. This validation provides a means to refine Griffith-Irwin descriptions beyond idealized interfaces to realistic hybrid materials and heterointerfaces where neither  $\gamma_p$  nor  $\gamma_a$  can be neglected.

Finally, by carrying out experiments similar to described above at different temperatures, we can obtain deformation mechanism maps for the interfacial delamination as a function of thermochemical variables such as temperature and water activity (see Fig. 5b). At all temperatures,  $\gamma_a$  increases with decreasing  $a_{\text{H}_2\text{O}}$  due to decreased hydroxylation-induced interfacial siloxane bridge weakening. At low  $a_{\text{H}_2\text{O}}$ ,  $\gamma_a$  is high, and  $\Gamma_{\text{FT}}$  increases with increasing temperature due to increased  $\gamma_p$ . At high  $a_{\text{H}_2\text{O}}$ ,  $\Gamma_{\text{FT}} \sim \gamma_a$  because the interfacial bonds are too weak to support copper plasticity;  $\gamma_a$  decreases with increasing

temperature due to facile bond breaking at elevated temperatures. Generation of interfacial deformation maps by our approach for other materials systems would open up new ways of studying the effects of thermochemical parameters on interfacial fracture to model phenomena such as stress corrosion cracking, stress- and electro-migration that are accentuated in devices and systems comprised of nanomaterials.

#### IV. CONCLUSIONS

In summary, we have demonstrated an experimental approach using molecular functionalization and environmental control to quantitatively partition the fracture energy  $\Gamma_{FT}$  of a heterointerface into work of adhesion  $\gamma_a$  and plastic energy  $\gamma_p$ . We employed a model metal-ceramic interface with a nanomolecular monolayer to force fracture to occur in a confined nanoscopic plane by breaking exactly one kind of interfacial bond whose strength can be adjusted by altering the chemical environment. This approach obviates uncertainties in crack path, and number and type of bonds broken, and allows the determination of the work of adhesion  $\gamma_a$  and extraction of plastic energy  $\gamma_p$  and its dependence on  $\gamma_a$ . Our results provide a means to quantitatively describe fracture energetics using the Griffith-Irwin model without neglecting either  $\gamma_p$  or  $\gamma_a$ . This framework obviates errors arising from neglecting either term and paves the way for rational design and accurate stability modeling of materials and structures comprised of heterointerfaces, e.g., composites, coatings, material joints, nanoelectronics devices and packaging. Additionally, it provides an alternative means for determining the ductile layer yield stress  $\sigma_y$ . Finally, our approach is attractive for adaptation for studying the effects of environmental degradation, segregation, and molecular functionalization on the nanomechanics of interfacial fracture in diverse materials systems through appropriate choice of nanomolecular layers and chemical environments.

#### V. ACKNOWLEDGEMENTS

This work was supported by a grant from the NSF through the award DMR 0519081 and a NRI-NIST grant through the Index Center at the University at Albany.



## FIGURE CAPTIONS

Figure 1. (a) Schematic sketch depicting water-induced siloxane bond breaking in an organosilane NML at a Cu/NML/silica interface. (b) A typical load-relaxation curve from a four point bend test with a schematic showing the crack path. A crack initiated at the notch tip on the substrate traverses to the weakest interface and propagates laterally at a constant load corresponding to  $\Gamma_c$  (green). When displacement is arrested, the crack is driven sub-critically by the remnant load (red) which continually decreases until crack growth stops. The remnant load at the crack arrest point corresponds to the equilibrium fracture toughness  $\Gamma_{FT}$ .

Figure 2. (a) Crack velocity  $v$  vs. the driving energy  $\Gamma$  plots obtained at  $T=278$  K at different  $a_{H_2O}$ . The red solid line represents the reaction rate kinetics model fit<sup>15</sup> for  $a_{H_2O} = 0.25$ . (b) Plot showing  $\Gamma_{FT}$  decrease with  $a_{H_2O}$  (blue) and temperature (green).

Figure 3. (a) Survey XPS spectra from silica fracture surfaces show Si and O peaks with no traces of Cu, while Cu fracture surfaces exhibit prominent Cu peaks (top). (b) Multiplex scans on Cu fracture surfaces show Si 2p signatures of silyl alkyl moieties ( $\sim 102.5$  eV) in the organosilane, in contrast to the silica band ( $\sim 103.5$  eV) on silica fracture surfaces (bottom left). This result, and the exclusive presence of S 2p peak on the Cu fracture surface (bottom right), indicate that delamination occurs via siloxane bond fissure at the NML-silica interface (top left—where filled green and red spheres denote Si and S, respectively, in the MPTMS NML). The essentially identical spectral features for  $0.05 \leq a_{H_2O} < 0.8$  (bottom left) indicate that the delamination path is unchanged. At  $a_{H_2O} \sim 0.8$ —the highest water activity in our experiments— Cu fracture surfaces exhibit a silica sub-band along with the prominent silyl alkyl signature, suggesting some fracture path deviation due to bond breaking in the silica substrate.

Figure 4. (a)  $\Gamma_{FT}$  as a function of  $a_{H_2O}$  at 293 K. Inset schematically illustrates  $\gamma_a$  and  $\gamma_p$ ; plasticity is depicted as wiggles in the delaminated Cu film. (b) Cu yield stress  $\sigma_y$  extracted from  $\Gamma_{FT} - \log a_{H_2O}$  plots (red) compared with that obtained by nanoindentation (blue), molecular dynamics simulations of nanograined bulk Cu<sup>24</sup> and extrapolation of an analytical model developed from nanoindentation of thicker films<sup>25</sup>. (c) The  $\Gamma_{FT}$  increase with Cu film thicknesses at constant  $a_{H_2O}$  where  $\gamma_p \neq 0$ .

Figure 5. (a) Plastic energy  $\gamma_p$  in copper plotted as a function of the interfacial work of adhesion  $\gamma_a$ , at  $T=293$  K. (b) Deformation mechanism map created from  $\Gamma_{FT}$  measurements on structures with Cu/NML/SiO<sub>2</sub> interfaces with a 100 nm-thick Cu film for  $278 \text{ K} \leq T \leq 358 \text{ K}$  and  $0.6 \leq a_{H_2O} \leq 0.1$ . In yellow/orange/red regions  $\gamma_p$  is a major contributor, while green and blue regions represent conditions where  $\Gamma_{FT} \sim \gamma_a$ .

## VI. REFERENCES

- <sup>1</sup> A. A. Griffith, *Philosophical Transactions of the Royal Society of London, Series A* **A221**, 98 (1920).
- <sup>2</sup> *Failure Analysis and Prevention* (ASM International, Materials Park, OH, 1975).
- <sup>3</sup> G. R. Irwin, *Fracture dynamics: Fracturing of metals* (American Society for Metals, Cleveland, OH, 1948).
- <sup>4</sup> J. W. Hutchinson, *J. Mech. Phys. Solids* **16**, 1 (1968).
- <sup>5</sup> M. Lane, R. H. Dauskardt, N. Krishna, and I. Hashim, *J. Mater. Res.* **15**, 203 (2000).
- <sup>6</sup> Z. Suo, in *Comprehensive Structural Integrity*, edited by W. Y. W. Gerberich (Elsevier, St. Louis, 2003), Vol. 8.
- <sup>7</sup> N. A. Fleck, J. W. Hutchinson, and Z. Suo, *Int. J. Solids Struct.* **27**, 1683 (1991).
- <sup>8</sup> K. K. Cameron and R. H. Dauskardt, *Scr. Mater.* **54**, 349 (2006).
- <sup>9</sup> D. D. Gandhi, M. Lane, Y. Zhou, A. P. Singh, S. Nayak, U. Tisch, M. Eizenberg, and G. Ramanath, *Nature* **447**, 299 (2007).
- <sup>10</sup> G. Ramanath, G. Cui, P. G. Ganesan, X. Guo, A. V. Ellis, M. Stukowski, K. Vijayamohanan, P. Doppelt, and M. Lane, *Appl. Phys. Lett.* **83**, 383 (2003).
- <sup>11</sup> J. J. Vlassak, Y. Lin, and T. Y. Tsui, *Mater. Sci. Eng. A* **391**, 159 (2005).
- <sup>12</sup> Q. Ma, *J. Mater. Res.* **12**, 840 (1997).
- <sup>13</sup> P. G. Charalambides, J. Lund, A. G. Evans, and R. M. McMeeking, *J. Appl. Mech.* **111**, 77 (1989).
- <sup>14</sup> P. R. Wiederhold, *Water vapor measurement* (Marcel Dekker Inc., New York, NY, 1997).
- <sup>15</sup> B. R. Lawn, *Fracture of Brittle Solids* (Cambridge University Press, Cambridge, 1993).
- <sup>16</sup> R. J. Charles, *A review of glass strength* (Pergamon Press, New York, 1961).
- <sup>17</sup> M. Lane, *Ann. Rev. Mater. Res.* **33**, 29 (2003).
- <sup>18</sup> R. F. Cook and E. G. Liniger, *J. Amer. Ceram. Soc.* **76**, 1096 (1993).
- <sup>19</sup> A. Perriot, D. Vandembroucq, E. Barthel, V. Martinez, L. Grosvalet, C. Martinet, and B. Champagnon, *J. Amer. Ceram. Soc.* **89**, 596 (2006).

- <sup>20</sup> J. R. Rice and T. R., *Phil. Mag. A* **29**, 73 (1974).
- <sup>21</sup> M. Lane, R. H. Dauskardt, A. Vainchtein, and H. J. Gao, *J. Mater. Res.* **15**, 2758 (2000).
- <sup>22</sup> V. Tvergaard and J. W. Hutchinson, *J. Mech. Phys. Solids* **40**, 1377 (1992).
- <sup>23</sup> *Properties and Selection: Nonferrous Alloys and Special-Purpose Materials* (ASM International, Materials Park, OH, 1990).
- <sup>24</sup> J. Schiotz and K. W. Jacobsen, *Science* **301**, 1357 (2003).
- <sup>25</sup> A. A. Volinsky, J. Vella, I. S. Adhietty, V. Sarihan, L. Mercado, B. H. Yeung, and W. W. Gerberich, *Mater. Res. Soc. Symp. Proc.* **649**, Q5.3.1 (2000).
- <sup>26</sup> V. Tvergaard and J. W. Hutchinson, *Phil. Mag. A* **70**, 641 (1994).
- <sup>27</sup> I. H. Lin and R. Thomson, *Acta Mater.* **34**, 187 (1986).
- <sup>28</sup> A. A. Volinsky, N. R. Moody, and W. W. Gerberich, *Acta Mater.* **50**, 441 (2002).
- <sup>29</sup> A. A. Volinsky, N. I. Tymiak, M. D. Kriese, W. W. Gerberich, and J. W. Hutchinson, *Mater. Res. Soc. Symp. Proc.* **539**, 277 (1999).
- <sup>30</sup> W. W. Gerberich, A. A. Volinsky, N. I. Tymiak, and N. R. Moody, *Mater. Res. Soc. Symp. Proc.* **594**, 351 (2000).

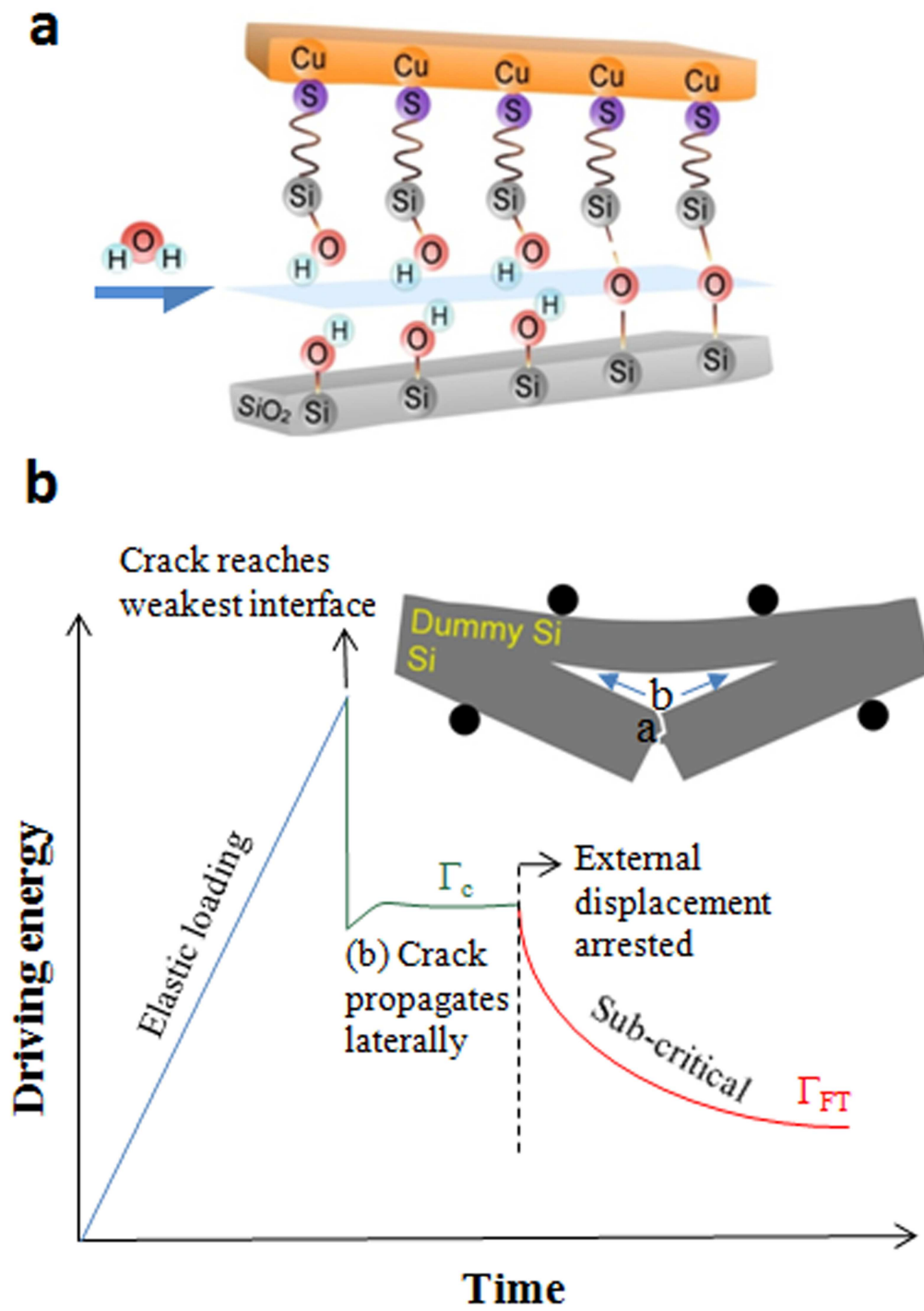


Figure 1

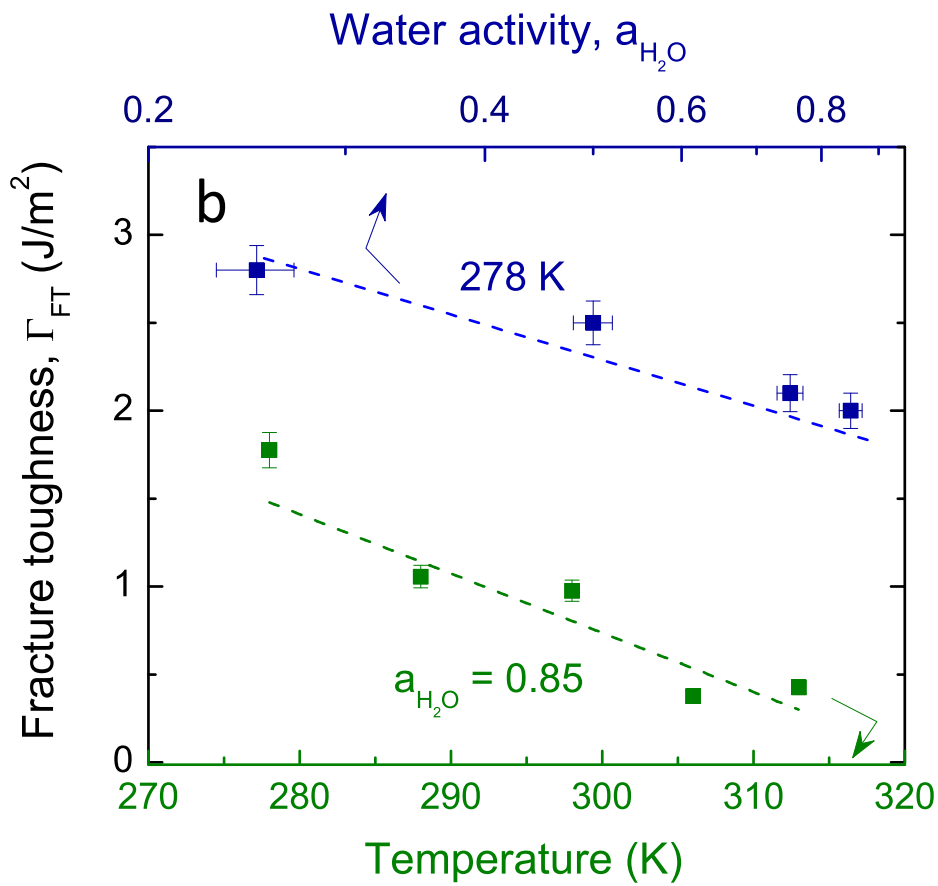
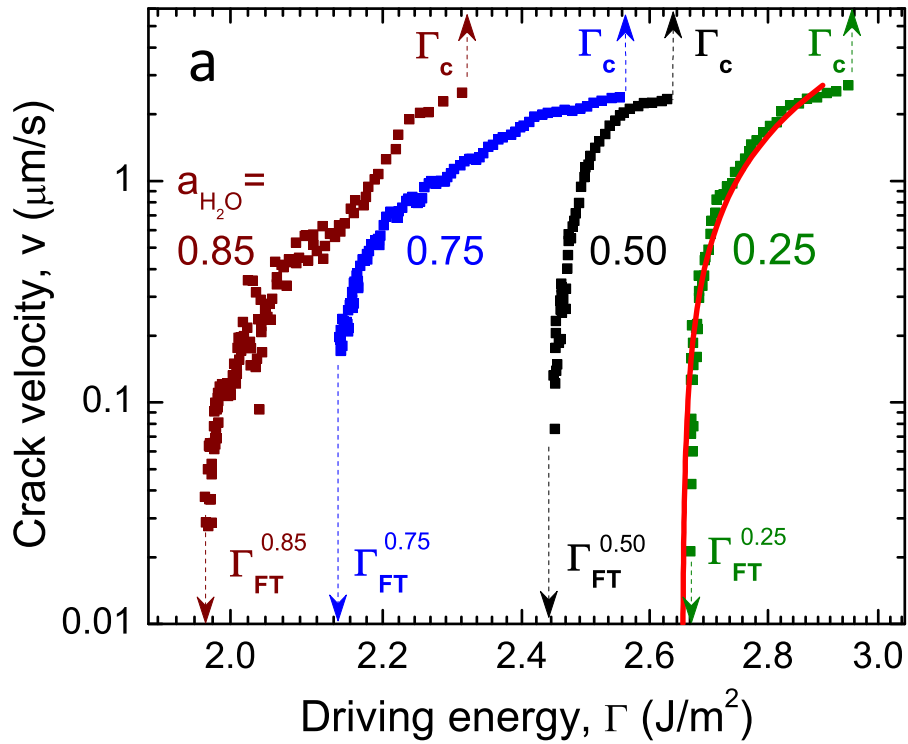


Figure 2

LN12213B

10NOV2010

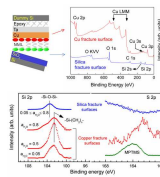
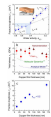


Figure 3

LN12213B

10NOV2010



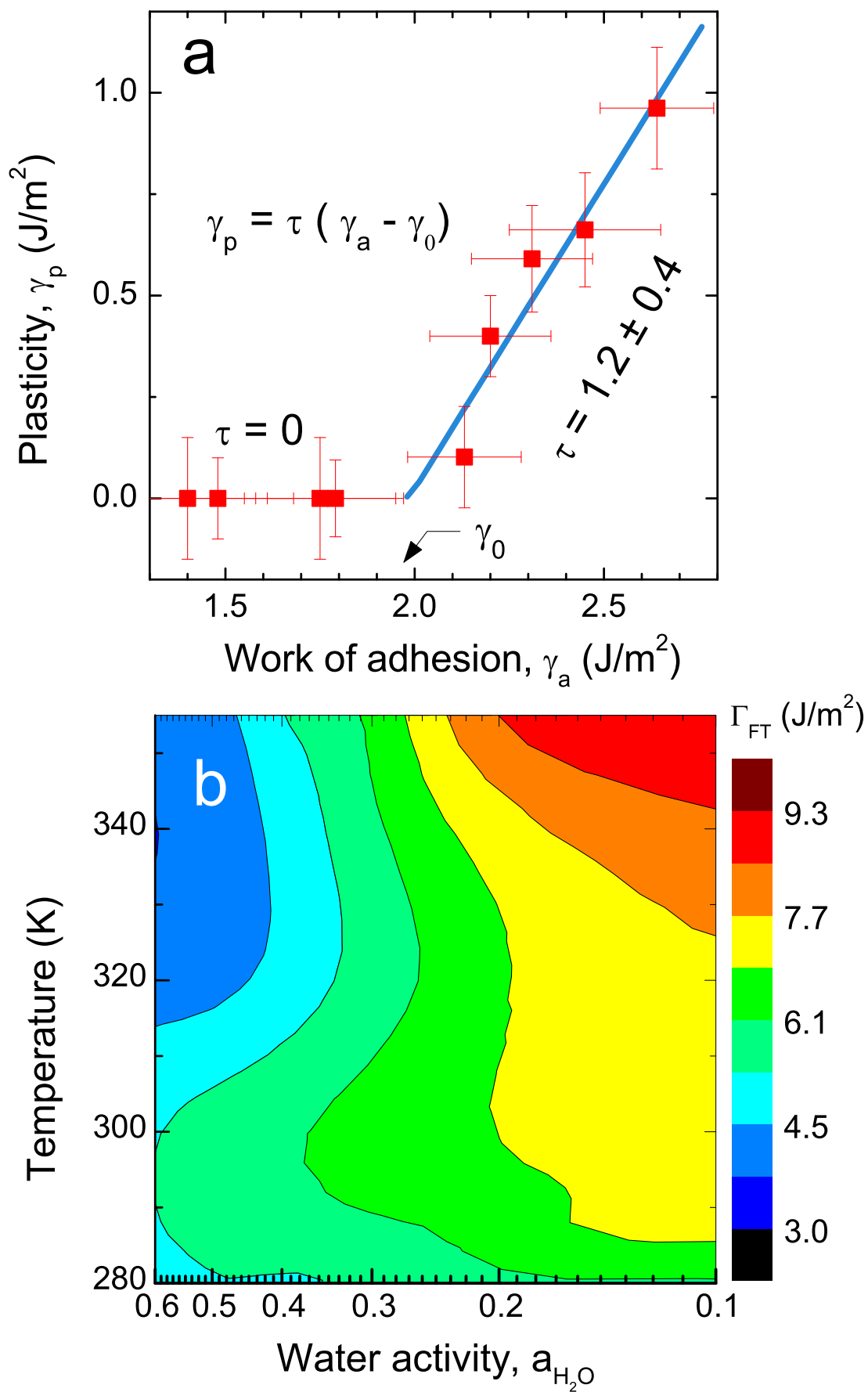


Figure 5

LN12213B

10NOV2010